Check for updates

Rapid Laser Processing of Thin Sr-Doped LaCrO$_{3-\delta}$ Interconnects for Solid Oxide Fuel Cells

Akihiro Ishii, Shenglong Mu, Yuqing Meng, Hua Huang, Jincheng Lei, Yanjun Li, Fei Peng, Hai Xiao, Jianhua Tong,* and Kyle S. Brinkman*

Rapid laser reactive sintering (RLRS) is an additive manufacturing process which enables the quick and efficient fabrication of a wide range of ceramic-based cells with various geometries and microstructures. Herein, the preparation of La$_{0.8}$Sr$_{0.2}$CrO$_{3-\delta}$ interconnects by RLRS for solid-oxide fuel/electrolysis cells (SOFC/ECs) is demonstrated. Uniform perovskite structure without residual intermediate phases can be achieved by CO$_2$ laser irradiation at 103 W with a scanning speed of 0.07–0.10 mm s^{-1}. Narrowing the width of the underlying MgO substrate and deposition of a terpineol-based slurry with a solid loading level of less than 4 g m^{-2} are found to be critical parameters to avoid cracking and delamination. The optimum laser conditions balance Cr loss and densification of La$_{0.8}$Sr$_{0.2}$CrO$_{3-\delta}$ resulting in an 11-μm-thick RLRS-derived La$_{0.8}$Sr$_{0.2}$CrO$_{3-\delta}$ film having a high relative density of 80–95% with a low area specific resistance (ASR) of 0.003 Ω cm^2 at 600 °C. This ASR is more than 30 times lower than that of furnace-sintered La$_{0.8}$Sr$_{0.2}$CrO$_{3-\delta}$ in the same thickness range. The RLRS technique is promising for quick and efficient preparation of dense and thin La$_{0.8}$Sr$_{0.2}$CrO$_{3-\delta}$ which are key components for highly compact SOFC/ECs.

1. Introduction

Solid-oxide fuel cells (SOFCs) and their reverse operation, solid-oxide electrolysis cells (SOECs), are a key technology for highly efficient generation of electricity and hydrogen.[1–3] The cells are composed of an electrolyte and two electrodes exposed to oxidizing/reducing gases and are electrically connected by an interconnect material. A large body of work has been established around these four components for almost five decades to discover the best materials and processing techniques.[3,4] For the interconnect material, perovskite-type acceptor-doped lanthanum chromite (La$_{1-x}$M$_x$CrO$_{3-\delta}$) has been a primary material of focus because of

following three reasons: sufficient electronic conductivity (10^{-2}–10^2 S cm^{-1}),[5–8] chemical stability over a wide oxygen partial pressure range from 10^{-21} to 10^0 atm,[8,9] and compatibility of the thermal expansion coefficient (TEC) of $\approx 1 \times 10^{-5}$ K^{-1} with that of the underlying SOFC/EC electrodes.[8,10,11] Ca or Sr are often selected as the acceptor dopant on the La site, leading to thermally activated hopping conduction of p-type small polarons.[5,8,11,12] Although several alloys have attracted interest as an interconnect material due to lower operating temperature for SOFC/ECs,[1,8,13] LaCrO$_3$ has retained the leading role as the interconnect material of choice due to its appropriate set of the conductivity, stability, and TEC.[8,14–18]

The LaCrO$_3$ interconnect is required to be dense and thin to separate the oxidizing and reducing gases while minimizing the resistance between components. However, it is well-known that LaCrO$_3$ has very poor sinterability[10,19–21] due to its high melting point (2465 °C[22]) and the evaporation of CrO$_3$ during sintering.[20,23] In the case of conventional solid-state sintering, Mori et al. has reported that the relative density of lanthanum chromite is less than 70% even after sintering at 1600 °C for 20 h.[10] To improve the sinterability, the following techniques can be used: sintering under reducing environment,[19,23,24] adding sintering aids or eutectic forming compounds,[23,25–28] using fine powder derived from metal nitrates,[28,29] and using sacrificing Cr sources.[30] However, multiple firing steps and high temperatures around 1600 °C for long durations are still generally needed even with these techniques. In addition, sintering aids have been shown to increase the TEC[11,12,27] and the use of costly nitrate precursors have proven problematic for practical applications.

This study focuses on a rapid laser reactive sintering (RLRS) technique as a new method to prepare dense and thin acceptor-doped LaCrO$_{3-\delta}$ interconnect materials. RLRS is a part of an additive manufacturing process using scanning lasers which can quickly give thermal energy required for phase formation and sintering of ceramics.[31–34] RLRS combined with computer-aided 3D printing will enable the fabrication of highly compacted multilayered structures with complicated geometric configuration of planer and tubular micro-SOFC/EC.[35] The authors' group recently demonstrated that RLRS can prepare dense films of BaZr$_{0.8}$Y$_{0.2}$O$_{3-\delta}$ and BaCe$_{0.7}$Zr$_{0.1}$Y$_{0.1}$Yb$_{0.1}$O$_{3-\delta}$,[36]

Dr. A. Ishii, S. Mu, Dr. Y. Meng, Dr. H. Huang, Prof. F. Peng, Prof. J. Tong, Prof. K. S. Brinkman
Department of Materials Science and Engineering
Clemson University
Clemson, SC 29634, USA
E-mail: jianhut@clemson.edu; ksbrink@clemson.edu

Dr. J. Lei, Dr. Y. Li, Prof. H. Xiao
Department of Electrical and Computer Engineering
Clemson University
Clemson, SC 29634, USA

The ORCID identification number(s) for the author(s) of this article can be found under https://doi.org/10.1002/ente.202000364.

DOI: 10.1002/ente.202000364

**ADVANCED
SCIENCE NEWS**
www.advancedsciencenews.com

Energy Technology
Generation, Conversion, Storage, Distribution
www.entechnol.de

which are well-known proton-conducting SOFC/EC electrolytes with poor sinterability.[37,38] $LaCrO_3$ also has poor sinterability due to evaporation of the Cr oxide during high-temperature and long-duration sintering; therefore, RLRS is an ideal technique to prepare dense and thin $LaCrO_3$. This study presents phases, microstructure, and electrical properties of RLRS-derived Sr-doped $LaCrO_{3-\delta}$ films as a function of laser conditions.

2. Results and Discussion

The RLRS mechanism relies on the introduction of thermal energy by a CO_2 laser; therefore, it is reasonable that laser conditions (e.g., power, scanning speed, defocus distance) and substrate properties (e.g., geometrical dimension, heat transfer coefficient, temperature) have significant effects on the properties. This study investigated appropriate ranges of the laser power and scanning speed for the RLRS of 7.5 ± 1.5 mg green $La_{0.8}Sr_{0.2}CrO_{3-\delta}$ slurry deposited on MgO pellets (ø14 mm, 2 mm thick) at fixed defocus distance (5 mm) and substrate temperature (550 °C) (The details are described in Section 4). **Figure 1**a shows samples appearance after the laser irradiation at various power and speed (70 W and 0.01 mm s^{-1}, 76, 82, 87, 92, 96 W and 0.10 mm s^{-1}, 100 W and 0.30 mm s^{-1}). At 0.10 mm s^{-1}, the sample color was changed from green to black as laser power was increased from 76 to 96 W, which

indicates perovskite-type $La_{0.8}Sr_{0.2}CrO_{3-\delta}$.[28,39] The formation of the perovskite-type $La_{0.8}Sr_{0.2}CrO_{3-\delta}$ was confirmed by X-ray diffraction (XRD) patterns as shown in Figure 1b. The XRD patterns of the black-colored samples are attributed to $La_{0.8}Sr_{0.2}CrO_{3-\delta}$, $MgCr_2O_4$, and MgO substrate. The predominant phase is $La_{0.8}Sr_{0.2}CrO_{3-\delta}$, with a secondary phase of $MgCr_2O_4$. The lattice parameter of the cubic-perovskite phase $La_{0.8}Sr_{0.2}CrO_{3-\delta}$ was calculated as 3.887 Å which is within 0.01% deviation from the reported value of furnace-sintered $La_{0.8}Sr_{0.2}CrO_{3-\delta}$.[39] Very weak XRD peaks (suggested with * in Figure 1b) are attributed to $La_{4.67}[SiO_4]_3O$,[40] which indicates a small amount of agate was contaminated during the ball-milling stage. These XRD patterns suggest that RLRS can prepare Sr-doped $LaCrO_{3-\delta}$ in a few minutes without residual intermediate phases (e.g., $SrCrO_4$,[10] $LaCrO_4$[41–43]).

It is worthwhile to identify a processing window of RLRS for $La_{0.8}Sr_{0.2}CrO_{3-\delta}$ because ultimately RLRS of the electrolyte, electrodes, and interconnect will be performed sequentially during device fabrication. The RLRS of $La_{0.8}Sr_{0.2}CrO_{3-\delta}$ was attempted under conditions of a weaker laser power and slower scanning speed (70 W and 0.01 mm s^{-1}) and a stronger laser power and faster scanning speed (100 W and 0.30 mm s^{-1}), respectively. However, the weaker and slower laser irradiation resulted in white-colored samples (Figure 1a) presumably due to the diffusion of Cr to MgO during long-time laser irradiation. This idea is supported by the XRD pattern of this sample
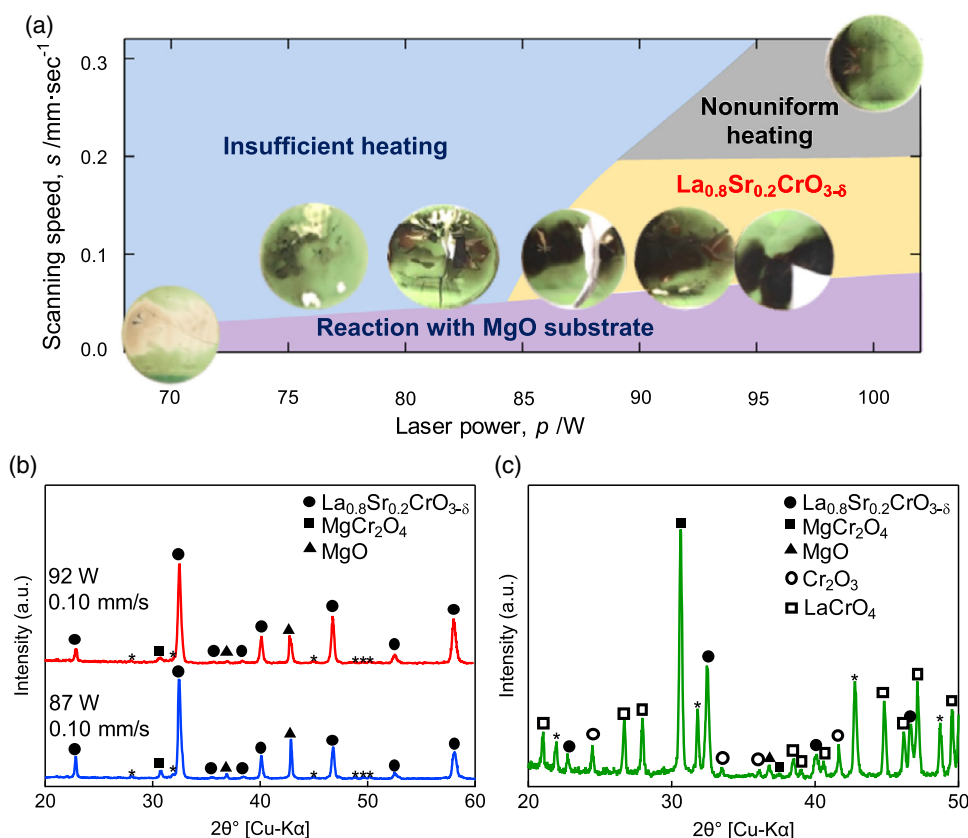

Figure 1. a) Sample appearance depending on laser power and scanning speed, and processing window for the RLRS of $La_{0.8}Sr_{0.2}CrO_{3-\delta}$ on MgO proposed by taking XRD patterns of the samples prepared at b) 87, 92 W, and 0.10 mm s^{-1} and c) 70 W and 0.01 mm s^{-1} into account. Laser scanning was conducted from right to left of each pellet. XRD patterns were taken only for the color-changed regions of the pellets.

showing the preferential formation of $MgCr_2O_4$ (Figure 1c). $LaCrO_4$ was also identified in this sample, indicating that thermal energy given by the laser irradiation at this condition is insufficient for the decomposition of $LaCrO_4$ to $LaCrO_3$.[42] Likewise, the stronger and faster laser condition was unsuitable for the RLRS of $La_{0.8}Sr_{0.2}CrO_{3-\delta}$ because the sample color changed only nearby the ending part of laser scanning (scanning was conducted from right to left). This is most likely because that the laser heating was not sufficient at beginning due to heat dissipation and became sufficient near completion of the scan by heat accumulation. Taking these results and the basic principle that stronger laser power and slower scanning speed gives greater thermal energy into consideration, this study proposes the processing window shown in Figure 1a. The RLRS of $La_{0.8}Sr_{0.2}CrO_{3-\delta}$ can be realized in the region of high power (>85 W) and moderate scanning speed (≈ 0.10 mm s^{-1}).

RLRS of $La_{0.8}Sr_{0.2}CrO_{3-\delta}$ was demonstrated as mentioned earlier; however, cracking of the samples was problematic. As the cracking is generally initiated by huge thermal gradient between laser irradiated/nonirradiated regions,[34,44] the width of the MgO substrate was reduced by polishing to be narrower than the laser beam width (≈ 10 mm). **Figure 2**a shows the picture of the $La_{0.8}Sr_{0.2}CrO_{3-\delta}$ film on the 6.5-mm-width MgO

bar after RLRS at 100 W and 0.10 mm s^{-1}. The cracking was successfully avoided using the 6.5-mm-width MgO bars as substrate. It is noted that the $La_{0.8}Sr_{0.2}CrO_{3-\delta}$ films delaminated from the MgO bars after RLRS regardless of the laser conditions when the green $La_{0.8}Sr_{0.2}CrO_{3-\delta}$ slurry deposited more than 4 g m^{-2} (4 mg for the MgO bars), as shown in Figure 2b. This is likely due to the lack of penetration by the CO_2 laser through the $La_{0.8}Sr_{0.2}CrO_{3-\delta}$ layer deposited at solid loadings in excess of 4 g m^{-2}. On the MgO bar, the sample color turned uniformly black after the RLRS at 100 W and 0.10 mm s^{-1} (Figure 2a); however, the sample contains the residue intermediate phase of $LaCrO_4$, as shown in Figure 2c. RLRS of $La_{0.8}Sr_{0.2}CrO_{3-\delta}$ with no intermediate phases was achieved above 103 W at 0.10 mm s^{-1} (Figure 2c). This power value is higher than the value utilized for MgO pellets (87 W, Figure 1), which is reasonable due to the width of the MgO bar as compared to the laser beam width.

In general, $LaCrO_3$-based materials have poor sinterability due to evaporation of CrO_3 during sintering at high temperature for long duration.[20,23] However, the high relative density can be expected for the RLRS-derived $La_{0.8}Sr_{0.2}CrO_{3-\delta}$ films because the RLRS process is completed in a few minutes without residual intermediate phases as shown earlier. **Figure 3** shows surface morphology of the $La_{0.8}Sr_{0.2}CrO_{3-\delta}$ films on the MgO bars after the RLRS at a) 98 W and 0.10 mm s^{-1}, b) 100 W and 0.10 mm s^{-1}, c) 103 W and 0.10 mm s^{-1}, d) 103 W and 0.08 mm s^{-1}, e) 103 W and 0.07 mm s^{-1}. Through an increase in the laser energy input from 98 W at 0.10 mm s^{-1} to 100 W at 0.10 mm s^{-1}, the morphology was drastically changed from a network structure (Figure 3a) to a micrograin-agglomerated structure (Figure 3b). This change was accompanied by the formation of the $La_{0.8}Sr_{0.2}CrO_{3-\delta}$ phase. Indeed, the micrograin-agglomerated structure is typical in acceptor-doped $LaCrO_{3-\delta}$.[29,39,45–47] Through further increase in the laser energy input (Figure 3c–e), the phase formation was completed, as shown in Figure 3c. In the samples prepared over these ranges of the laser conditions, no clear dependence of the grain size (1–3 μm) on the laser energy input was found, and their relative densities were varied.

To analyze the relative density in detail, an image analysis was conducted by GIMP[48] and ImageJ.[49] A location dependence of the relative density due to the Gaussian distribution of the laser
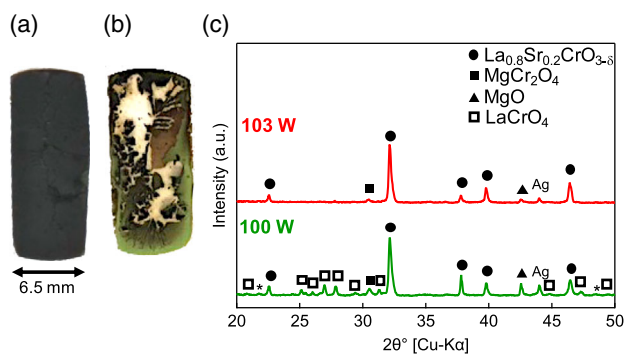

Figure 2. Samples appearance after RLRS of $La_{0.8}Sr_{0.2}CrO_{3-\delta}$ on MgO bars at a) 100 W and 0.10 mm s^{-1} and b) 87 W and 0.10 mm s^{-1}. c) XRD patterns of RLRS-derived $La_{0.8}Sr_{0.2}CrO_{3-\delta}$ films prepared at 100 W and 103 W (at 0.10 mm s^{-1}). Ag is current corrector.

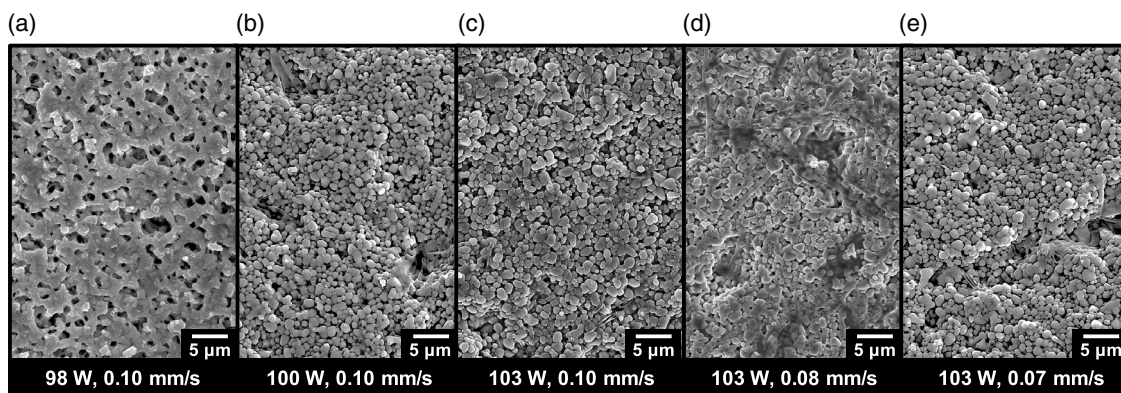**Figure 3.** Surface SEM images of the $La_{0.8}Sr_{0.2}CrO_{3-\delta}$ on MgO bars after RLRS at a) 98 W and 0.10 mm s^{-1}, b) 100 W and 0.10 mm s^{-1}, c) 103 W and 0.10 mm s^{-1}, d) 103 W and 0.08 mm s^{-1}, and e) 103 W and 0.07 mm s^{-1}.

ADVANCED
SCIENCE NEWS
www.advancedsciencenews.com

Energy Technology
Generation, Conversion, Storage, Distribution
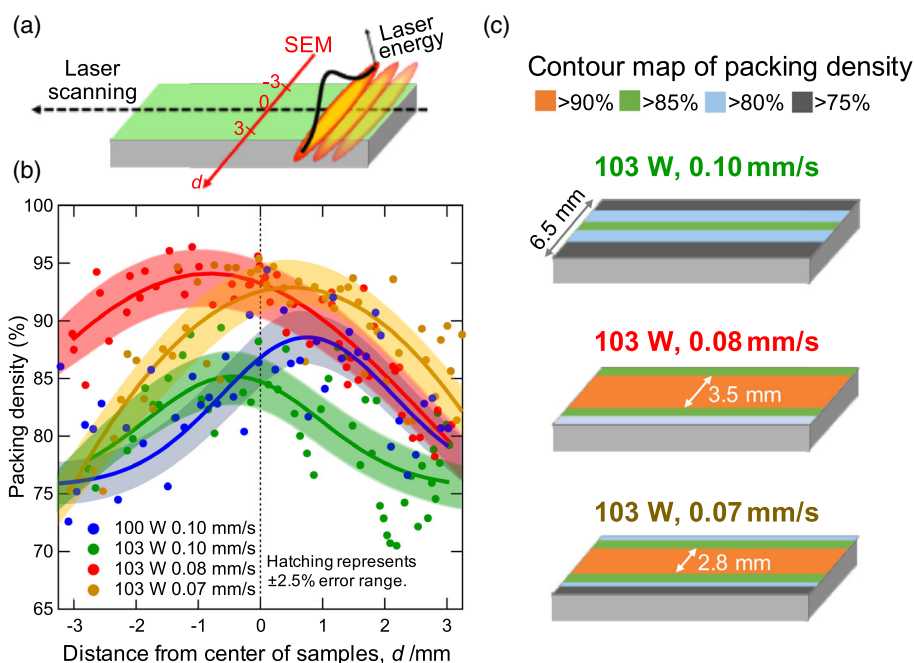www.entechnol.de

Figure 4. a) Geometrical relation between laser scanning and SEM observation directions, b) location dependence of relative density, and c) schematic contour diagram of the relative density distribution.

beam intensity was assumed as shown in **Figure 4**a. The relative density of the samples were analyzed as a function of the location by taking surface scanning electron microscopy (SEM) images at the center of the samples while changing location (d) perpendicular to the laser scanning direction. Figure 4b shows the distribution of the relative density and its Gaussian curve fittings. It is noted that the mismatch of the sample center and the center of the density distribution originates from errors in sample alignment (sample manually aligned). It was revealed that with increased laser power the relative densities of the samples were decreased (from 100 to 103 W at 0.10 mm s^{-1}), followed by an increase (from 0.10 to 0.08 mm s^{-1} at 103 W), and were then subsequently decreased (from 0.08 to 0.07 mm s^{-1} at 103 W). It is believed that this behavior is a result of phase conversion of a LaCrO$_4$ phase to the LaCrO$_3$-based phase (see Figure 2c), the densification of the LaCrO$_3$-based phase, and Cr sublimation (explained later), respectively. The phase conversion from LaCrO$_4$ to LaCrO$_3$ can lead to a decrease in the relative density because LaCrO$_4$ occupies 1.29 times more space than LaCrO$_3$ (cf. theoretical density of LaCrO$_4$ and LaCrO$_3$ are 5.00 and 6.46 g cm^{-3}). Using this data, the relative density distribution of the samples having no LaCrO$_4$ phase was schematically depicted as Figure 4c. The highly densified regions become the widest at 0.08 mm s^{-1} (approximately 3.5 mm for >90%, 5.7 mm for >85%, and 7.2 mm for >80% of relative density). This degree of the densification is higher than the relative density of the La$_{0.8}$Sr$_{0.2}$CrO$_{3-\delta}$ films sintered using furnaces at 1400 °C in air (60–70%[30]).

The decrease in the relative density by slowing the scanning speed from 0.08 to 0.07 mm s^{-1} is most likely due to Cr loss. **Figure 5** shows cross-sectional SEM images and their energy dispersive spectrometer (EDS) mapping of Mg and Cr for

the La$_{0.8}$Sr$_{0.2}$CrO$_{3-\delta}$ films on the MgO bars prepared at a) 0.08 mm s^{-1} and b) 0.07 mm s^{-1}. These SEM images were taken at their highly densified regions (>90%). In these regions, both La$_{0.8}$Sr$_{0.2}$CrO$_{3-\delta}$ films were well-densified in the thickness (≈11 μm) direction as well as the surface direction. Their EDS mappings of Mg indicates that the both La$_{0.8}$Sr$_{0.2}$CrO$_{3-\delta}$ films contain a certain amount of Mg; however, the Mg content is overestimated in these mapping images because of peak overlapping with La. Figure 5 shows the Cr content which was higher in the La$_{0.8}$Sr$_{0.2}$CrO$_{3-\delta}$ films prepared at a) 0.08 mm s^{-1} than at b) 0.07 mm s^{-1}. There are two possible reasons for this Cr loss: 1) diffusion of Cr^{3+} and Mg^{2+} between the deposition and the MgO substrate, and 2) volatilization of Cr^{3+}. The former reason is the most likely because higher Mg content in the sample prepared at 0.07 mm s^{-1} was suggested by XPS (4.5 and 8.4%Mg for 0.08 and 0.07 mm s^{-1}). As this Cr loss and the densification of the La$_{0.8}$Sr$_{0.2}$CrO$_{3-\delta}$ are balanced, the laser-operation condition of 103 W and 0.08 mm s^{-1} results in a La$_{0.8}$Sr$_{0.2}$CrO$_{3-\delta}$ film with the highest relative density.

Low surface area-specific resistance (ASR) is required for the La$_{0.8}$Sr$_{0.2}$CrO$_{3-\delta}$ interconnect performance; otherwise, the ohmic loss of the SOFC/EC is increased, resulting in decreased energy conversion efficiency. As ASR is given by thickness divided by conductivity, high conductivity and small thickness are important parameters which determine ASR. The conductivity of the RLRS-derived La$_{0.8}$Sr$_{0.2}$CrO$_{3-\delta}$ films is shown as an Arrhenius-type plot in **Figure 6**a. They show explicit negative linear relationship, which is consistent when conduction is due to a thermally activated hopping mechanism as reported.[5,8,11,12] The increase in the conductivity at increased laser power from 98 to 103 W (with 0.10 mm s^{-1}) is due to enhanced formation of the targeted La$_{0.8}$Sr$_{0.2}$CrO$_{3-\delta}$ phase. The conductivity was further increased
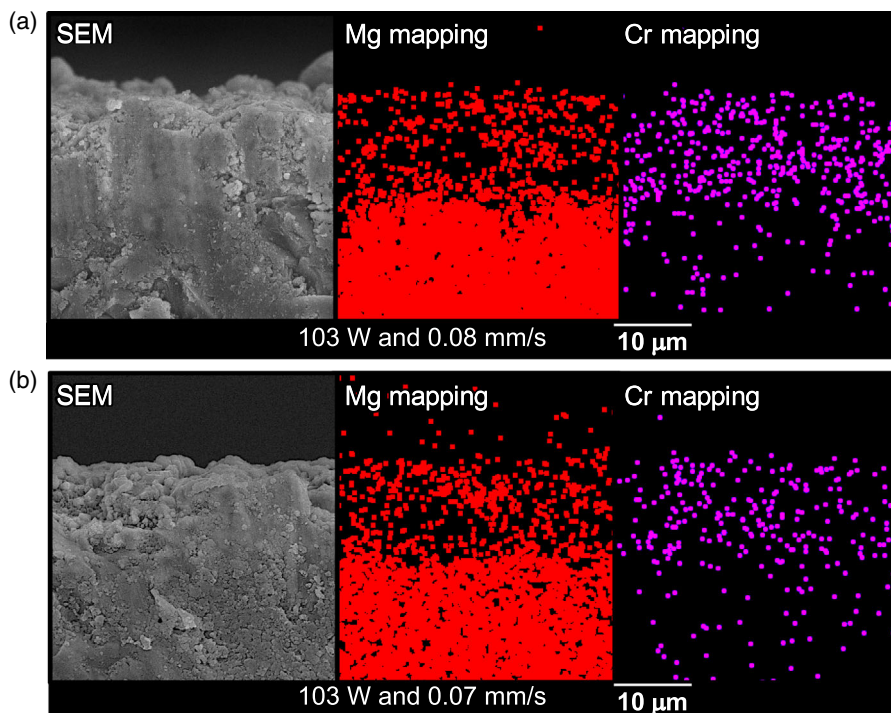
Figure 5. Cross-sectional SEM images and EDS mapping of the $La_{0.8}Sr_{0.2}CrO_{3-\delta}$ on MgO bars after RLRS at a) 103 W and 0.08 mm s^{-1}, and b) 103 W and 0.07 mm s^{-1}.
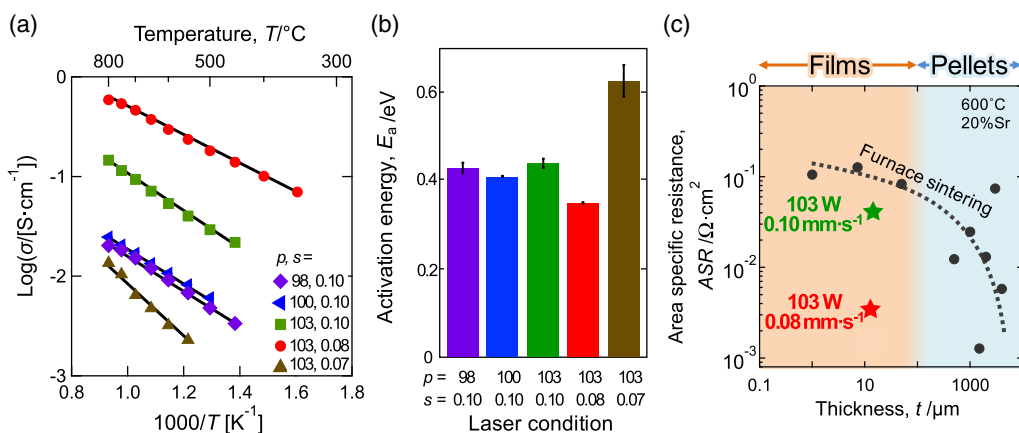

Figure 6. a) Conductivity, b) activation energy, and c) ASR at 600 °C of RLRS-derived $La_{0.8}Sr_{0.2}CrO_{3-\delta}$ films prepared at a power, p [W], and a speed, s [mm s^{-1}]. ASR of furnace-sintered $La_{0.8}Sr_{0.2}CrO_{3-\delta}$[50–56] are also shown for comparison.

and then decreased by slowing the scanning speed down to 0.08 and 0.07 mm s^{-1} (with 103 W). This is because the relative density reaches to maximum (80–95%, Figure 4) at 0.08 mm s^{-1}. As shown in Figure 6b, the lowest activation energy (0.35 eV) can also be obtained at 0.08 mm s^{-1}. These values of conductivity are approximately 10^2 lower than those of highly densified ($\approx$95% relative density) $La_{0.8}Sr_{0.2}CrO_{3-\delta}$ pellets sintered using the furnace in a controlled environment.[50,51] This difference is most likely as a result of that, for the RLRS-derived $La_{0.8}Sr_{0.2}CrO_{3-\delta}$ films, the density has in-plane variations perpendicularly to the laser scanning direction (80–95% from edge to center in the case at 0.08 mm s^{-1} with 103 W,

Figure 4c) and the Cr site are partially (4.5%) substituted by less conductive Mg.

Figure 6c shows the relation between ASR and sample thickness. ASR of the furnace-sintered $La_{0.8}Sr_{0.2}CrO_{3-\delta}$ was collected from literature.[50–56] Ideally, ASR can be decreased by decreasing the thickness. However, data from furnace-sintered $La_{0.8}Sr_{0.2}CrO_{3-\delta}$ reveal the opposite trend. The origin of this phemenon is believed due to increased specific surface area in thinner samples resulting in enhanced Cr volatalization. The ASR of the 11-μm-thick RLRS-derived $La_{0.8}Sr_{0.2}CrO_{3-\delta}$ film prepared at 103 W and 0.08 mm s^{-1} is 3×10^{-3} Ω cm^2 was more than 30 times lower than that of the furnace-sintered

Table 1. Process and property comparison between laser/furnace-sintered $La_{0.8}Sr_{0.2}CrO_{3-\delta}$ and coated alloy. Data in references[51,57,58] was used. ASR was calculated using thickness and conductivity.

Materials	Process	Sintering time	Thickness [μm]	Conductivity (600 °C) [S cm^{-1}]	ASR (600 °C) [Ω cm^2]	TEC ($\times 10^6$) [K^{-1}]
$La_{0.8}Sr_{0.2}CrO_{3-\delta}$	Laser sintering	≈3 min (for 14 mm long)	11	3×10^{-1}	3×10^{-3}	–
$La_{0.8}Sr_{0.2}CrO_{3-\delta}$	Furnace sintering (1900 °C)	1 h	500	4×10^1	1×10^{-2}	9.9
Coated ferritic stainless steel	Furnace sintering (800 °C)	100 h	11 (coating)	1×10^4 (steel)	6×10^{-5}	11.4
				2×10^1 (coating)		

$La_{0.8}Sr_{0.2}CrO_{3-\delta}$ in the same thickness range. In other words, the thinly made $La_{0.8}Sr_{0.2}CrO_{3-\delta}$ prepared by the RLRS method shows more than 30 times lower ASR than samples prepared using conventional furnace sintering. This is believed due to the rapid laser sintering processssing, which can minimize Cr volatilization. In addition, the ASR of the RLRS interconnect is also 25–30 times lower than the values for the state-of-the-art SOFC/EC electrodes and electrolyte.[1]

In **Table 1**, the RLRS-derived $La_{0.8}Sr_{0.2}CrO_{3-\delta}$ is compared with currently widely accepted two interconnect materials, the furnace-sintered $La_{0.8}Sr_{0.2}CrO_{3-\delta}$[51] and ferritic stainless steel coated with conductive passivation layer,[57,58] in terms of process and properties. The furnace-sintered $La_{0.8}Sr_{0.2}CrO_{3-\delta}$ has been intentionally studied due to its conductivity and compatible TEC in comparison with other SOFC/EC components. The alloy system has received increased attention in recent years as the working temperature of SOFC/EC have decreased SOFC/EC and composition-controlled ferric stainless steels coated with Mn and Co-based spinels have been found as an interconnect material showing excellent ASR and relatively low TEC among metals.[57] However, a long-duration aging treatment is required to manipulate the metal-oxide interface and delamination from the SOFC/EC electrodes has been reported due to its high TEC as compared to ceramics.[59] The laser sintering process paves the way for preparation of dense and thin $La_{0.8}Sr_{0.2}CrO_{3-\delta}$ beyond the current thickness limitation by virtue of its rapid processing. The authors are actively engaged in trials on the preparation of thin $La_{0.8}Sr_{0.2}CrO_{3-\delta}$ by RLRS on real SOFC/EC electrodes including exploring the use of diffusion blocking materials to passivate inter-diffusion between the $La_{0.8}Sr_{0.2}CrO_{3-\delta}$ and the electrode materials during RLRS. The RLRS technique is a promising technique for quick and efficient preparation of dense and thin $La_{0.8}Sr_{0.2}CrO_{3-\delta}$ which are key components for highly compact SOFC/ECs. It is expected that the RLRS technique will be useful for preparation of a wide range of ceramic-based films. The process is fundamentally able to densify thin-film materials containing volatile elements due to the rapid nature of the process.

3. Conclusion

RLRS of $La_{0.8}Sr_{0.2}CrO_{3-\delta}$ films on MgO was demonstrated using a CO_2 laser. Uniform perovskite structure with no delamination and no residual intermediate phases was achieved in the range of 0.10–0.07 mm s^{-1} at 103 W by narrowing the substrate width to thickness less than the laser beam width (10 mm) and by

deposition of the terpineol-based green $La_{0.8}Sr_{0.2}CrO_{3-\delta}$ slurry at solid loading levels less than 4 g m^{-2}. The optimum laser condition balanced densification and Cr loss, resulting in the 11-μm-thick RLRS-derived $La_{0.8}Sr_{0.2}CrO_{3-\delta}$ film showing high relative density of 80–95% and low ASR of 0.003 Ω cm^2 at 600 °C. This resistance is more than 30 times lower than that of the furnace-sintered $La_{0.8}Sr_{0.2}CrO_{3-\delta}$ in this thickness range. As evaporation of CrO_3 can be minimized by the RLRS technique, high-performing $LaCrO_3$-based materials may soon become the interconnect materials of choice for next-generation SOFC/EC devices.

4. Experimental Section

The laser sintering apparatus is schematically shown in **Figure 7**a. CO_2 laser ($\lambda = 10.6$ μm, Ti100W, Synrad) was reflected by gold mirrors (reflectance >99% at $\lambda = 10.6$ μm, NB1-L01, Thorlabs, Inc.) twice to be directed to samples perpendicularly. A cylindrical focal lens (focal length 25.4 cm, diameter 19.05 mm, Laser Mechanisms, Inc.) was utilized to increase laser beam width. The focal lens was placed at 5 mm defocus position, resulting in approximately 10 mm of laser beam width. Samples were preheated to 550 °C by a hot plate to mitigate thermal shock during RLRS. Actual laser power as a function of laser-controlling power percentage was measured in this configuration. As shown in Figure 7b, the percentage, x, can be converted to laser power, p, by following equation

$$p = -7.5 \times 10^{-5} x^3 + 4.9 \times 10^{-3} x^2 + 1.34x \tag{1}$$

The error bar in Figure 7b, which is ±5% of the power, represents fluctuation of laser power and accuracy of a power meter (PW-250, SYNRAD, Inc.). One-line scanning was conducted at several speeds.

RLRS of 20 mol% Sr-doped $LaCrO_{3-\delta}$ ($La_{0.8}Sr_{0.2}CrO_{3-\delta}$) was performed on MgO substrate. MgO was chosen because it is an electrical insulator
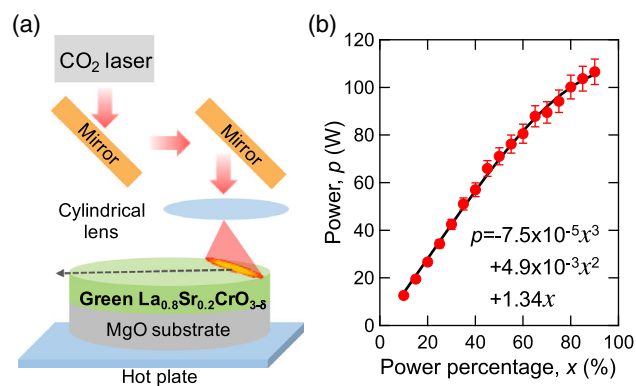

Figure 7. a) Schematic picture of laser sintering apparatus, and b) relation between power percentage and actual laser power.

and is compatible with La_2O_3.[60] Although MgO reacts with Cr_2O_3, forming Cr-substituted MgO and spinel-type $MgCr_2O_4$,[47,61] these reactions are practically limited during RLRS of $LaCrO_3$ because of limited solubility of Cr^{3+} in MgO (≈2 mol% even at its eutectic point) and high melting point of $MgCr_2O_4$ (2405 °C). RLRS of $LaCrO_3$ had also attempted on $3(La_2O_3)\cdot WO_3$, which has been reported as compatible with $LaCrO_3$ by Polfus et al.;[62] meanwhile, intense chemical reaction between $3(La_2O_3)\cdot WO_3$ and Cr_2O_3 was confirmed during RLRS of $LaCrO_3$. A 2-mm-thick MgO substrate was prepared by pelletizing MgO powder (Across Organics, purity 99.99%) at 188 MPa by a uniaxial pressing machine followed by sintering at 1500 °C for 10 h. This condition gives relative density higher than 94%. On the MgO substrate, terpineol-based green $La_{0.8}Sr_{0.2}CrO_{3-\delta}$ slurry was deposited by drop coating. The slurry was prepared by a planetary ball milling of stoichiometric amount of La_2O_3 (Tokyo Chemical Industry Co., Ltd., purity >99.9%), Cr_2O_3 (Alfa Aesar, purity 99.97%), and $SrCO_3$ (Sigma Aldrich, purity $\geq$99.9%) with α-terpineol (Across Organics, purity >97%) at 400 rpm for 12 h using agate jars and balls. The weight ratio of the ceramic powders and terpineol was controlled to 1:6 for uniform deposition by drop coating. The authors attempted to use water-based slurry; however, La_2O_3 turned into $La(OH)_3$ by the chemical reaction with water, which led to delamination of the $La_{0.8}Sr_{0.2}CrO_{3-\delta}$ layer, most likely due to significant volume change during RLRS (cf. La_2O_3 and $La(OH)_3$ are 40.2 Å$^{3[63]}$ and 71.2 Å$^{3[64]}$ per La atom). The authors also attempted to use $La_2(CO_3)_3$ and Cr metal instead of La_2O_3 and Cr_2O_3. However, $La_2(CO_3)_3$ reacted with air moisture and then resulted in delamination (cf. $La_2(CO_3)_3\cdot8H_2O$ and $LaOHCO_3$ are 365.8 Å$^{3[65]}$ and 76.7 Å$^{3[66]}$ per La atom), and the slurry consisting of Cr metal could not be heated well as compared to Cr_2O_3 due to the higher reflectance of as-compared to oxides at the wavelength of the CO_2 laser.[67] After drop coating, the specimens were dried at 150 °C for 15 min using a hot plate.

Phases of the samples were analyzed by XRD (MiniFlex600, Rigaku). XRD patterns were collected by θ–2θ continuous scans using Cu-Kα radiation ($\lambda = 1.5406$ Å). Microstructure of the samples were observed by field emission scanning electron microscope (FE-SEM) combined with EDS (S-4800, Hitachi). Pt was coated on the samples by DC sputtering (Hummer 6.2, Anatech Ltd.) for 2 min under 80 mTorr to prevent charging up during SEM observation. Mg content in the samples was analyzed by X-ray photoelectron spectroscopy (XPS, PHI 5000 VersaProbe III, ULVAC-PHI, Inc.) XPS peak positions were corrected using a carbon 1 s reference set at 284.80 eV. Mg 1s and Cr 2p spectra were used for compositional analysis. Temperature dependence of four-probe DC resistibility was measured using multimeter (Model 2001, Keithley Instruments, Inc.). The configuration of the four probes are schematically shown in **Figure 8**. The direction of current flow was in the longitudinal direction of the samples. The distance between the inner two probes was measured by the image analysis in each sample. Ag paste (T-20GM, Heraeus) and Ag wire (ø0.1 mm, Alfa Aesar) were utilized as a current corrector and for connection between the samples and the multimeter. The samples were heated up to 800 °C and then were stepwisely cooled down by 50 °C. The resistibility was measured after maintaining the samples at each temperature for 30 min.
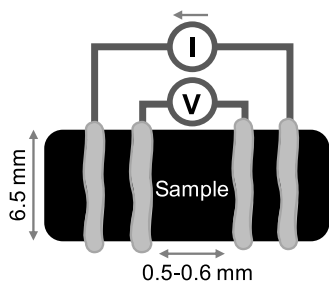

Figure 8. Configuration of four-probe measurement.

Conflict of Interest

The authors declare no conflict of interest.

[1] C. Duan, J. Tong, M. Shang, S. Nikodemski, M. Sanders, S. Ricote, A. Almandoori, R. O'Hayre, *Science* **2015**, *349*, 1321.

[2] J.-H. Myung, D. Neagu, D. N. Miller, J. T. S. Irvine, *Nature* **2016**, *537*, 528.

[3] L. Bi, S. Boulfrad, E. Traversa, *Chem. Soc. Rev.* **2014**, *43*, 8255.

[4] S. C. Singhal, *Solid State Ionics* **2000**, *135*, 305.

[5] D. P. Karim, A. T. Aldred, *Phys. Rev. B* **1979**, *20*, 2255.

[6] K. Azegami, M. Toshinaka, K. Hirota, O. Yamaguchi, *Mater. Res. Bull.* **1998**, *33*, 341.

[7] K. P. Bansal, S. Kumari, B. K. Das, G. C. Jain, *J. Mater. Sci.* **1983**, *18*, 2095.

[8] W. Z. Zhu, S. C. Deevi, *Mater. Sci. Eng. A* **2003**, *348*, 227.

[9] T. Nakamura, G. Petzow, L. J. Gauckler, *Mater. Res. Bull.* **1979**, *14*, 649.

[10] M. Mori, Y. Hiei, N. M. Sammes, *Solid State Ionics* **2000**, *135*, 743.

[11] J. W. Fergus, *Solid State Ionics* **2004**, *171*, 1.

[12] M. Mori, Y. Hiei, *J. Am. Ceram. Soc.* **2004**, *84*, 2573.

[13] Y. Meng, J. Gao, Z. Zhao, J. Amoroso, J. Tong, K. S. Brinkman, *J. Mater. Sci.* **2019**, *54*, 9291.

[14] N. Shaigan, D. G. Lvey, W. Chen, *J. Power Sources* **2008**, *183*, 651.

[15] N. Shaigan, D. G. Lvey, W. Chen, *J. Power Sources* **2008**, *185*, 331.

[16] N. Shaigan, W. Qu, D. G. Lvey, W. Chen, *J. Power Sources* **2010**, *195*, 1529.

[17] J. H. Zhu, Y. Zhang, A. Basu, Z. G. Lu, M. Paranthaman, D. F. Lee, E. A. Payzant, *Surf. Coat. Technol.* **2004**, *177*, 60.

[18] C. Johnson, R. Gemmen, N. Orlovskaya, *Compos. B Eng.* **2004**, *35*, 167.

[19] L. Groupp, H. U. Anderson, *J. Am. Ceram. Soc.* **1976**, *59*, 449.

[20] Y. Ren, W. Ma, X. Li, J. Wang, Y. Bai, H. Dong, *Mod. Phys. Lett. B* **2016**, *30*, 1650127.

[21] D. Rubio, C. Suciu, I. Waernhus, A. Vik, A. C. Hoffmann, *J. Mater. Process. Technol.* **2017**, *250*, 270.

[22] P. Perrot, G. Effenberg, MSIT, The La2O3-Cr2O3 quasibinary system, https://materials.springer.com/msi/phase-diagram/docs/sm_msi_r_10_010535_01_full_LnkDia1 (accessed: March 2020).

[23] H. Yokokawa, N. Sakai, T. Kawada, M. Dokiya, *J. Electrochem. Soc.* **1991**, *138*, 1018.

[24] M. Mori, T. Yamamoto, T. Ishikawa, Y. Takeda, *Solid State Ionics* **2002**, *148*, 93.

[25] B. K. Flandermeyer, R. B. Poeppel, J. T. Dusek, H. U. Anderson, USA US4749632A, **1988**.

[26] R. Koc, H. U. Anderson, *J. Eur. Ceram. Soc.* **1992**, *9*, 285.

[27] S. P. Simner, J. S. Hardy, J. W. Stevenson, T. R. Armstrong, *Solid State Ionics* **2000**, *128*, 53.

[28] R. Subasri, T. Mathews, K. Swaminathan, O. M. Sreedharan, *J. Alloys Compd.* **2003**, *354*, 193.

[29] X. Ding, Y. Liu, L. Gao, L. Guo, *J. Alloys Compd.* **2008**, *458*, 346.

[30] A. Heidarpour, G. M. Choi, M. H. Abbasi, A. Saidi, *J. Alloys Compd.* **2012**, *512*, 156.

[31] A. Manthiram, D. L. Bourell, H. L. Marcus, *J. Miner. Met. Mater. Soc.* **1993**, *45*, 66.

[32] L. F. Ji, Y. J. Jiang, *Appl. Phys. A* **2007**, *87*, 733.

[33] M. Okutomi, M. Kasamatsu, K. Tsukamoto, S. Shiratori, F. Uchiyama, *Appl. Phys. Lett.* **1984**, *44*, 1132.

[34] B. Qian, Z. Shen, *J. Asian Ceram. Soc.* **2013**, *1*, 315.

[35] A. Zhakeyev, P. Wang, L. Zhang, W. Shu, H. Wang, J. Zuan, *Adv. Sci.* **2017**, *4*, 1700187.

[36] S. Mu, Z. Zhao, J. Lei, Y. Hong, T. Hong, D. Jiang, Y. Song, W. Jackson, K. S. Brinkman, F. Peng, H. Xiao, J. Tong, *Solid State Ionics* **2018**, *320*, 369.

[37] K. D. Kreuer, *Solid State Ionics* **1999**, *125*, 285.

[38] L. Yang, S. Wang, K. Blinn, M. Liu, Z. Liu, Z. Cheng, M. Liu, *Science* **2009**, *326*, 126.

[39] P. S. Devi, M. S. Rao, *J. Solid State Chem.* **1992**, *98*, 237.

[40] P. Villars, La9.33(SiO4)6O2 (La4.67[SiO4]3O) Crystal Structure, http://materials.springer.com/isp/crystallographic/docs/sd_1101733 (accessed: March 2020).

[41] E. Povoden, M. Chen, A. N. Grundy, T. Ivas, L. J. Gauckler, *J. Phase Equilib. Diffus.* **2009**, *30*, 12.

[42] T. J. Kallarackel, S. Gupta, P. Singh, *J. Am. Ceram. Soc.* **2013**, *96*, 3933.

[43] H. Konno, H. Tachikawa, A. Furusaki, R. Furuichi, *Anal. Sci.* **1992**, *8*, 641.

[44] S. L. Sing, W. Y. Yeong, F. E. Wiria, B. Y. Tay, Z. Zhao, L. Zhao, Z. Tian, S. Yang, *Rapid Prototyping J.* **2017**, *23*, 611.

[45] Z. Han, J. Liu, X.-W. Li, Y.-X. Chen, G.-H. Liu, J.-T. Li, *J. Am. Ceram. Soc.* **2014**, *97*, 2705.

[46] J. G. M. Furtado, R. N. Oliveira, *Materia* **2008**, *13*, 147.

[47] S. P. Jiang, L. Liu, K. P. Ong, P. Wu, J. Li, J. Pu, *J. Power Sources* **2008**, *176*, 82.

[48] S. Kimball, P. Mattis, The GIMP team, GNU Image Manipulation Program 2.10.10, https://www.gimp.org/ (accessed: March 2020).

[49] C. T. Rueden, J. Schindelin, M. C. Hiner, B. E. DeZonia, A. E. Walter, E. T. Arena, K. W. Eliceiri, *BMC Bioinf.* **2017**, *18*, 529.

[50] N. Gunasekaran, N. Bakshi, C. B. Alcock, J. J. Carberry, *Solid State Ionics* **1996**, *83*, 145.

[51] M. Mori, T. Yamamoto, H. Itoh, T. Watanabe, *J. Mater. Sci.* **1997**, *32*, 2423.

[52] S. Tanasescu, A. Orasanu, D. Berger, I. Jitaru, J. Schoonman, *Int. J. Thermophys.* **2005**, *26*, 543.

[53] X.-D. Zhou, I. Belogolovsky, B. J. Scarflno, S. Reis, R. K. Brow, P. Y. Hou, H. U. Anderson, *Proc. in 2004 ECS Meeting*, Texas, USA **2004**.

[54] K. Deshpande, A. Mukasyan, A. Varma, *J. Am. Ceram. Soc.* **2003**, *86*, 1149.

[55] E. L. Brosha, R. Mukundan, D. R. Brown, F. H. Garzon, Growth of lanthanum strontium citromium oxide thin films front fluoride sputtering process, https://www.osti.gov/servlets/purl/789483 (accessed: March 2020).

[56] T. Franco, Z. HoshiarDin, P. Szabo, M. Lang, G. Schiller, *J. Fuel Cell Sci. Technol.* **2007**, *4*, 406.

[57] Z. Yang, G.-G. Xia, X.-H. Li, J. W. Stevenson, *Int. J. Hydrogen Energy* **2007**, *32*, 3648.

[58] VDM Metals GmbH, Data Sheet-Crofer 22 APU, https://www.vdm-metals.com/fileadmin/user_upload/Downloads/Data_Sheets/Data_Sheet_VDM_Crofer_22_APU (accessed: March 2020).

[59] J. C. W. Mah, A. Muchtar, M. R. Somalu, M. J. Ghazali, *Int. J. Hydrogen Energy* **2017**, *42*, 9219.

[60] P. Villars, La-Mg-O Vertical Section of Ternary Phase Diagram, http://materials.springer.com/isp/phase-diagram/docs/c_0210242 (accessed: March 2020).

[61] P. Villars, Cr-Mg-O Vertical Section of Ternary Phase Diagram, http://materials.springer.com/isp/phase-diagram/docs/c_0207260 (accessed: March 2020).

[62] J. M. Polfus, W. Xing, M.-L. Fontaine, C. Denonville, P. P. Henriksen, R. Bredesen, *J. Membr. Sci.* **2015**, *479*, 39.

[63] P. Villars, La2O3 Crystal Structure, http://materials.springer.com/isp/crystallographic/docs/sd_0303903 (accessed: March 2020).

[64] P. Villars, La(OH)3 (La[OH]3) Crystal Structure, http://materials.springer.com/isp/crystallographic/docs/sd_0313483 (accessed: March 2020).

[65] P. Villars, La2(CO3)3·8H2O (La2[CO3]3[H2O]8) Crystal Structure, http://materials.springer.com/isp/crystallographic/docs/sd_1002807 (accessed: March 2020).

[66] P. Villars, LaOHCO3 (La[CO3][OH] hex) Crystal Structure, http://materials.springer.com/isp/crystallographic/docs/sd_1253263 (accessed: March 2020).

[67] N. K. Tolochko, Y. V. Khlopkov, S. E. Mozzharov, M. B. Ignatiev, T. Laoui, V. I. Titov, *Rapid Prototyping J.* **2000**, *6*, 155.